Size-controlled wurtzite zinc oxide spheres with the characteristics of visible absorption and Mie scattering†

Ting-Ting Chen,[a] I-Chun Chang,[a] Min-Chiao Tsai,[a] Yi-Chun Chang,[b] Min-Han Yang,[a] Po-Chin Chen,[b] Hsin-Tien Chiu[b] and Chi-Young Lee*[a]

The enhancement of the light harvesting efficiency over a metal oxide is crucial to optic-related applications which can convert solar energy into chemical energy. Here, we demonstrated a method to develop the characteristics of visible light absorption and visible Mie scattering over wurtzite ZnO microspheres. Size-controlled ZnO microspheres were successfully prepared in the thermal decomposition of amorphous/layered basic zinc salt (LBZ) spheres. Firstly, trisodium citrate was employed as the chelating agent to synthesize amorphous/LBZ microspheres in a nucleation-controlled method. The sphere size was controlled by the nuclei number, which depends on the competition between hydroxyl ions and citrate to the ligand with Zn^{2+}. Secondly, visible-active wurtzite ZnO spheres were obtained by thermal decomposition. The uniform sized microspheres exhibited Mie scattering in the visible range due to the interaction with specific incident electromagnetic radiation, and the full absorption spectrum was easily obtained by tuning the size of the spheres. Such uniform spheres exhibited superior visible absorption and scattering effects and thus are expected to be good candidates for the optic-related applications.

Introduction

The augmentation of the light utilization efficiency over a metal oxide is crucial to design new solar energy conversion devices, such as dye-sensitized solar cells,[1–5] H_2 evolution,[6–8] and photocatalysis.[9–14] Various research has been focused on the promotion of the light utilization efficiency. The optical band gap narrowing of a metal oxide by defects or impurities has been used to promote visible light absorption.[9,11–16] In addition, the Mie scattering effect of spherical particles has also been introduced to lengthen the path of the incident light, improving the light harvesting efficiency.[4,8,10] The Mie scattering effect is the optical phenomenon which describes the particular incident electromagnetic wave which is redirected due to periodical perturbation in the electron cloud of uniform spherical objects with the same frequency as the electric field of the incident wave.[17–21] Theoretically, metal oxide spheres with these two optical properties can be fascinating materials to efficiently convert solar energy into chemical energy.

Recently, many studies have focused on spherically structured ZnO, which is an attractive material for various applications,

such as dye-sensitized solar cells,[1] photocatalysis,[10] and UV-photodetectors.[22] It has been reported that the visible-active ZnO can be prepared by the thermal decomposition of zinc hydroxide/amorphous compounds.[23,24] The sol–gel process with the assistance of chelating agents has usually been applied to synthesize zinc hydroxide/amorphous compounds with spherical structures. The chelating agents, such as trisodium citrate[25–29] and histidine,[30] can form complexes with Zn^{2+} and play an important role in the morphology control. It is likely that a minority of the zinc ions are free ions which can react with hydroxyl ions to form nanoclusters. Van der Waals interactions between the surface molecules of the nanocluster act as the driving force for self-assembly and result in a spherical structure with reduced surface energy.[31]

However, usually it is more difficult to control the size and uniformity of metal oxide spheres than the morphologies. The synthesis of zinc hydroxide/amorphous microspheres (~1 μm) with good uniformity and perfect spherical structures (no connection between the spheres) still remains a big challenge. During the reaction, the equilibrium between the solution components governs the formation of uniform colloidal particles in solution.[32,33] It has been reported that the one-step nucleation-controlled method was developed to synthesize uniform Cu_2O nanocubes with tunable sizes.[32] Trisodium citrate was employed as the chelating agent to form a copper–citrate complex which retards the precipitation of $Cu(OH)_2$ during the addition of NaOH, resulting in a lower

[a] *Department of Materials Science and Engineering, National Tsing Hua University, Hsinchu 30013, Taiwan, Republic of China. E-mail: cylee@mx.nthu.edu.tw*
[b] *Department of Applied Chemistry, National Chiao Tung University, Hsinchu 30010, Taiwan, Republic of China*
† Electronic supplementary information (ESI) available. See DOI: 10.1039/c3ce42370k

seed number. Larger Cu_2O nanocubes were obtained by increasing the amount of sodium citrate in the reaction solution. Well-controlled particle size can be achieved through the equilibrium between OH^- and citrate to the ligand with Cu^{2+}.

In this work, we demonstrated a new approach to produce size-tunable wurtzite ZnO spheres with visible light absorption and Mie scattering properties. Firstly, we adopted the nucleation-controlled method to prepare amorphous/layered basic zinc salts (LBZ) spheres with tunable sizes by using hexamethylenetetramine (HMTA) and trisodium citrate as a hydroxyl ion supplier and chelating agent, respectively. Here, the size of the spheres was controlled by the concentration of HMTA, which was proportional to the nuclei number. Secondly, the amorphous/LBZ spheres were further annealed and then converted into visible-active wurtzite ZnO spheres. Furthermore, as the uniform spheres could scatter specific incident light, the full absorption spectrum was easily obtained by tuning the size of the spheres. The formation mechanism and optical behavior of the spherical structures were systematically investigated.

Experimental

All the chemicals were analytical-grade reagents and used without further purification. In a typical experiment, an aqueous solution of 15 mM zinc acetate dihydrate (Zn $(CH_3COO)_2 \cdot 2H_2O$), 6 mM trisodium citrate and 40–140 mM hexamethylenetetramine (HMTA, 40, 60, 80, 100, 120, 130, and 140 mM, respectively) was refluxed at 115 °C for 1 h. After the reflux reaction, the white powder in the solution was collected by filtering, washing and drying in an oven at 50 °C and the thus obtained products were named as S4, S6, S8, S10, S12, S13 and S14 respectively. The as-synthesized samples (S4, S8, S12 and S14) were further annealed at 500 °C for 1 h with a ramp up rate of 4 °C min^{-1} under an air gas flow (50 sccm), and the thus obtained products were named as S4a, S8a, S12a and S14a, respectively.

The morphology of the powder was investigated using a field emission scanning electron microscope (FE-SEM, Joel-6500, 15 kV) and a transmission electron microscope (TEM, JEM-ARM200FTH, 200 kV). The crystal structure of the samples was characterized by powder X-ray diffraction (Brucker D8-advanced with Cu Kα radiation λ = 1.5405981 Å). A fourier transform infrared spectrometer (FT-IR, Bruker vertex series, powder mixed with KBr and compacted to pellets) was used to measure the transmission spectra. In order to investigate the Mie scattering behavior, the powder was coated onto transparent plastic slides by doctor-blade, and a UV-vis absorption spectroscope (Avantes) was utilized. The reflectance absorption spectrum of the powder was also recorded on a UV-vis spectroscope.

Results and discussion

Characterization of the amorphous/LBZ spheres

Fig. 1a–c are the SEM images of the S4, S12 and S14 samples respectively, which comprise a large amount of uniform
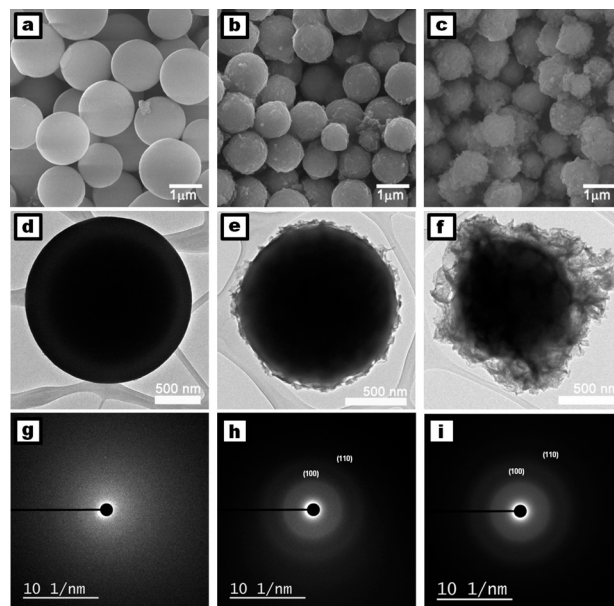

Fig. 1 SEM images of the (a) S4 (b) S12 (c) S14 spheres. The corresponding TEM images (d) (e) (f) and SAED (g) (h) (i).

spheres. The sphere size was reduced by increasing the concentration of HMTA in the reflux reaction at 115 °C, although the surface roughness increased (see also Fig. S1 in the ESI,†). The average diameters of the S4, S12 and S14 spheres were about 1.65, 1.22 and 0.98 μm, respectively. Fig. 1a shows that S4 with the largest diameter has a clean and glossy surface. In contrast, S14 with the smallest diameter displays a rough and deformed surface which is composed of irregular sheets, as shown in Fig. 1c. EDS analysis shows the C, O, and Zn signals from the as-synthesized samples (Zn ~15 wt%, O ~34 wt%, and C ~50 wt%, and the EDS analysis is summarized in Table S1, ESI†). The XRD patterns in Fig. S2 in the ESI† reveal that the crystallinity of the spherical structure increased with the HMTA concentration as the size of sphere was reduced. S4 (red line) is amorphous, whereas S14 (purple line) shows additional diffraction peaks located at 33.3° and 59.0°.

These very weak peaks correspond to the brucite-like structure indexed as (100) and (110), implying the presence of layered basic zinc salts (LBZ).[26,34–37] LBZ is a modified brucite structure which is composed of water molecules and inorganic or organic anions between positively charged polynuclear zinc hydroxyl layers for charge balance.[26] The broad and asymmetric peak located at 33.3° was attributed to the disorderly stacked zinc hydroxide layers along the *a* and *b* axes, which leads to destruction of the symmetry of the (*hk*0) diffraction peaks.[26,34–37]

The structural characterization obtained by using transmission electron microscopy (TEM) provides additional information about the interior and exterior structure of these spheres, as shown in Fig. 1d–f. It was found that S4 is a ~1.8 μm diameter solid sphere with a smooth and neat surface, as clearly shown in Fig. 1d. The selected area electron diffraction pattern (SAED, Fig. 1g) shows that S4 is nearly amorphous (these samples were unstable under electron irradiation),[25,35] which

is consistent with the XRD patterns. However, the TEM image of S14 presents a core–shell structure. The coarse solid core with a diameter of about 0.80 μm was coated with an irregular shell which consisted of fine thin sheets, as displayed in Fig. 1f. Furthermore, the TEM analysis indicates that the exterior shell exhibits a characteristic polycrystalline structure with slight and obscure diffraction rings of the (100) and (110) planes, corresponding to the LBZ structure. This result agrees with the XRD pattern, which displays the very weak diffraction peaks (purple line) in Fig. S2 in the ESI.† These results indicate that more crystalline and smaller spheres with a core–shell structure were obtained with higher concentrations of HMTA.

Fig. 2 and S3 in the ESI† are the IR spectra of these samples. Fig. 2a, c and e display a broad and strong absorption band at *ca.* 3400 cm^{-1} which is due to the stretching vibration of the hydroxyl group and water. A very weak absorption band at 2850–3000 cm^{-1}, which is nearly hidden by the strong absorption of the hydroxyl group, can be ascribed to a methyl group stretching vibration. Fig. 2b, d and f show strong absorption peaks at ~1600 cm^{-1} which can be assigned to asymmetric vibration of the carboxylic group $v_{as}(COO^-)$. The absorption band at 1450 cm^{-1} originates from a carboxylic group symmetric vibration $v_s(COO^-)$, methyl group deformation, and hydroxyl group bending vibration. No signal was observed at the range of 1700–1720 cm^{-1}, corresponding to the typical absorption bands of the carbonyl group of carboxylic acid.[25,27] This indicates that each carboxylic acid group is deprotonated. The presence of CH_2 and coordinated carboxylic groups in the IR spectrum of the S4 amorphous spheres suggested that the citrate groups were coordinated with Zn^{2+}, which is similar

to earlier studies. It has been reported that amorphous microspheres were synthesized by using zinc nitrate, HMTA, and citrate as reactants, and strong carboxylic group vibration signals in the IR spectra could be attributed to the coordinated citrate with Zn^{2+}.[25–27]

As the concentration of HMTA increased, the additional peaks at 1459, 1614, and 2922 cm^{-1} were observed, as shown in Fig. 2e and f. The IR spectrum of S14 reveals that the additional peaks due to the presence of CH_3 groups and coordination between the carboxylic groups and Zn^{2+}. This is related to the coordination of the acetate groups to Zn^{2+} in the LBZ structure.[25,27,35,38] In the case of S14, the exterior shell exhibits a characteristic LBZ crystalline structure, which is a construction of positively charged zinc hydroxyl layers, intercalated acetate groups and water molecules. Thus, these additional peaks of $v_{as}(COO^-)$ and $v_s(COO^-)$ can be ascribed to the coordination of the acetate groups to Zn^{2+}, which suggests the presence of LBZ. This result agrees with the TEM image of S14, which shows clearly that disordered LBZ shells conceal a coarse solid core.

Proposed formation mechanism of the size-controlled amorphous/LBZ spheres

According to the above observations, the sizes and morphologies of the spheres strongly depend on the concentration of the reactants.[39,40] HMTA is known as a mild basic agent to supply OH^- in the syntheses of diverse ZnO nanostructures. HMTA slowly releases OH^- during the reaction, and Zn^{2+} directly reacts with OH^- to form zinc hydroxide species as the building blocks for crystalline ZnO rods with a wurtzite phase (Fig. S4, ESI†). Citrate, which is one of the more common chelating agents, reacts with metal ions to form stable coordination complexes, and thus plays an important role in the formation of hierarchical metal oxides. In previous studies, amorphous random sized zinc citrate spheres and LBZ nanostructures were synthesized with the addition of trisodium citrate as the chelating agent.[25–29]

In a high citrate content solution, the $Zn(citrate)_2^{4-}$ complex (two equivalent citrate ions coordinate to one Zn^{2+}) is the dominated species and restrains the formation of wurtzite ZnO.[37] Moreover, the formation of a Zn^{2+}–citrate complex that strongly depends on the OH^- concentration is related to the nucleation of spheres.[25] As HMTA was added into the reaction, the released OH^- from HMTA influences the coordination between citrate and Zn^{2+} during the reaction. The discharged Zn^{2+} from the Zn^{2+}–citrate complex reacts with OH^- to form the nuclei of amorphous spheres. However, the synthesis of uniform spheres with tunable sizes has rarely been reported in the literature.

Herein, the nucleation-controlled method was adopted to control the size of the spheres. The seeding number of the spheres will be controlled by the competition between OH^- and citrate ions to the ligand with Zn^{2+}. As the concentration of zinc acetate and sodium citrate are fixed, the seeding number depends on the HMTA concentration. The increase in
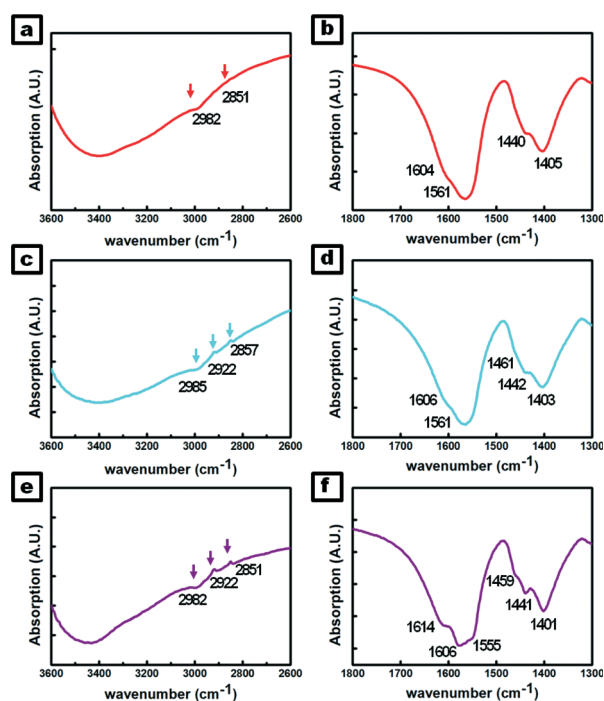

Fig. 2 FT-IR spectra of (a,b) S4 (c,d) S12 (e,f) S14.

HMTA enhances the discharge of Zn^{2+} and generates more nuclei for the spheres, leading to the formation of smaller spheres, as shown in Fig. S1 in the ESI.† The sizes of the spheres were 1.65 and 0.98 μm as the HMTA concentration was 40 and 140 mM, respectively. Furthermore, nanospheres were obtained by increasing OH^- using pre-heated HMTA (at 90 °C for 30 minutes) (Fig. S5, ESI†). Briefly, sized-controlled spheres can be easily obtained by nucleation-controlled growth using chelating agents.

The uniformity of the spheres can be controlled by the distribution of chemical complex species in the solution, which depends on the molar ratio of the reactants.[32,33] The ratio of $[Zn^{2+}]/[citrate]$ has an influence on the distribution of free and chelated Zn^{2+} in the solution, and the formation of the LBZ phase.

Fig. S6 in the ESI† shows the SEM images and XRD patterns of the samples synthesized with 40 mM HMTA and a Zn^{2+}/citrate molar ratio of 5. It indicates that the high Zn^{2+}/citrate molar ratio leads to the formation of irregular hierarchical structures with a highly crystalline LBZ phase, which is unfavorable to the uniformity of the morphology and leads to a poor distribution of the spheres.

In addition, the formation of LBZ sheets was further studied in detail. It was reported that amorphous spheres serve as native templates and are sacrificed for the formation of crystalline metal oxide/hydroxide hierarchical structures through an Ostwald ripening process.[27,28,41] Under a high HMTA concentration (>80 mM), spheres with an LBZ exterior shell and amorphous interior solid core were obtained. During the reaction, the unstable amorphous spheres become a template for the hierarchical structure of LBZ. Dissolution of the amorphous spheres from the smooth surface followed by the deposition of crystalline LBZ sheets proceeds spontaneously. During a further aging at 90 °C for 60 min, an amorphous solid sphere was etched gradually and continuously from the surface and finally transformed to a hollow sphere which consists of LBZ sheets only (Fig. S7, ESI†). A schematic diagram of the proposed formation mechanism of the amorphous/LBZ spherical structure has been displayed in Fig. 3.

Thermal decomposition of the amorphous/LBZ spheres

In general, thermal decomposition of metal hydroxides results in the formation of metal oxides without a morphological change, and has been used to synthesis crystalline metal oxide spheres.[23,24,35] The thermal behavior of the amorphous/LBZ spheres decomposing into ZnO was investigated by TGA. The TGA profiles of the samples presented in Fig. S8a in the ESI† show that the mass of the samples remains constant at ~380 °C. A gradual weight loss at temperatures below 300 °C is related to the dehydration of physically adsorbed water, and the weight loss at ~350 °C is attributed to the removal of organic content.

The amorphous/LBZ S4, S12, and S14 spheres were annealed at 500 °C for 1 h under an air flow, and the thus obtained products were named as S4a, S12a, and S14a
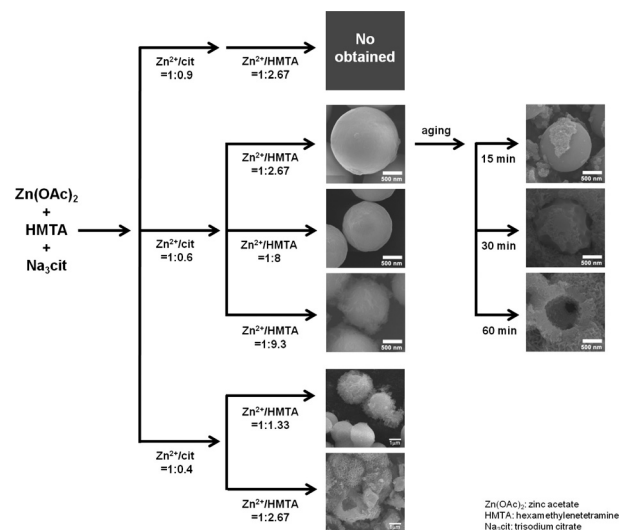

Fig. 3 Scheme of the proposed formation mechanism of the amorphous/LBZ spherical structure.

respectively. Fig. 4a–c shows that all the spheres remained spherical in shape but shrunk in size. The average diameters of the S4a, S12a and S14a spheres were about 1.21, 0.81 and 0.74 μm, respectively. The crystalline structure of the samples was further characterized by XRD. The XRD diffraction patterns in Fig. 4d reveal that all the annealed samples are highly crystalline with characteristic diffraction peaks at 31.7°, 34.4° and 36.2°, which correspond to the wurtzite phase (JCPDS 36-1451) and are indexed as (100), (002) and (101), respectively. The average grain sizes of S4a, S12a and S14a are 24.9 nm, 26.8 nm and 23.0 nm respectively, determined using Scherer's formula. Fig. S8b in the ESI† displays the TEM image of S4a. A solid sphere with polycrystalline wurtzite ZnO was evidenced by the
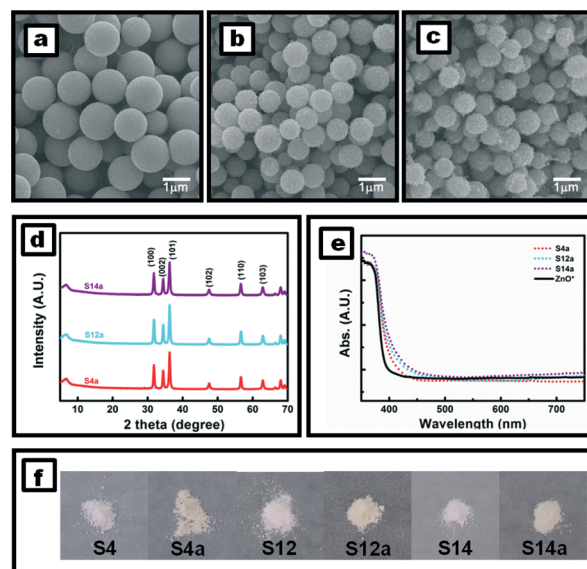

Fig. 4 SEM images of (a) S4a (b) S12a (c) S14a. (d) XRD patterns and (e) UV-vis reflectance absorption spectrum of the annealed spheres. (f) Photograph of the various-sized spheres before and after thermal decomposition.

inset SAED pattern with the three major planes {100}, {002} and {101}. Fig. S8c in the ESI† shows the Raman spectra of the ZnO spheres. The fundamental modes at ~330, 380, 438, 560 and 580 cm^{-1} are assigned to the E_2^{high}–E_2^{low}, A_1 (TO), E_2^{high}, A_1 (LO) and E_1 (LO) of wurtzite ZnO, respectively.[31,42] In particular, the E_1 (LO) mode, caused by the formation of defects such as oxygen vacancies, zinc interstitial or these complexes, reveals the presence of defects in the ZnO spheres.[42]

The ZnO sphere powder was yellow cream after annealing, and the UV-vis reflectance absorption spectra are displayed in Fig. 4e and f. The obvious band tail at 400–500 nm observed for all the ZnO spheres corresponds to the visible light absorption. This absorption can originate from defects (EDS analysis yielded O and Zn signals and thus the effect of impurities can be neglected).[42] The type of defects in the ZnO spheres was subsequently investigated in further detail using photoluminescence (PL) spectroscopy. Fig. S8d in the ESI† presents the PL spectrum of the samples with He–Cd laser excitation (325 nm). The strong and broad green emission at ~525 nm is typically associated with oxygen vacancies, whereas the sharp emission at ~382 nm is attributed to a band edge transition.[43] The presence of oxygen vacancies could be responsible for the band tail and the enhancement of the visible light absorption of the ZnO.

Mie scattering behavior of the amorphous/LBZ spheres

Inorganic spherical structures with a diameter of about 1 μm exhibit interesting optical properties. As the size of a spherical object approaches the wavelength of incident light, the resonance effect takes place, and is mainly confined to the surface of the object, known as Mie's scattering.[18–21]

Fig. 5a shows a photograph of a transparent plastic film that was coated with the various sized spheres, displaying a white color as is common for ZnO powder. When a back light was turned on, different vivid colors were observed due to the light scattering by the spheres, as shown in Fig. 5b (scattering angle > 0°). The coated plastic film with powders of S4, S6, S8, S10, S12, S13, and S14 displayed red, orange, yellow, green,

cyan, blue, and purple colors respectively. The full absorption spectrum can be achieved by tuning the size of the spheres.

According to the literature, forward scattering of incident light, namely, zero angle scattering (scattering angle = 0°), by amorphous TiO_2 spheres was determined by the local minimum of the absorption in the UV-vis spectra.[20] In order to understand more details about the scattering properties of these spheres, the UV-vis spectra were utilized to interpret the colors that we observed from the coated transparent plastic films. Fig. 6a and b are the absorption spectra of the spheres at scattering angles of θ = 0° and 5.7°, respectively. Apparently, wave-like curves, illustrated in Fig. 6, give strong evidence for the highly uniformity of the spheres in this work. Otherwise, the spectra present flat lines instead of wave-like curves with size polydispersity over 10%.[19]

The angular dependence of the Mie scattering influences the local absorption minimum at different scattering angles in the spectra. For example, Fig. S9a in the ESI† shows the absorption spectra of S4 at scattering angles of θ = 0° and 5.7°. The wavelength of the forward scattering of incident light (scattering angle = 0°, solid line in Fig S9a in the ESI†) by the S4 spheres is about ~500 nm, which was determined by the local minimum of the absorption in the UV-vis spectrum. The enhancement in light intensity of ~500 nm in the forward direction results from the resonance between the S4 spheres and the incident light with a wavelength of ~500 nm. It leads to the local minimum of absorption in the UV-vis spectra. Thus, a blue color was observed due to the light scattering by the S4 spheres when turning on a back light with a scattering angle = 0° (it was very difficult to take a good picture due to the very strong incident light). On increasing the scattering angle, the decreased flux of the forward scattering light leads to the increase of absorption. The local minimum absorption in the UV-vis spectrum (scattering angle = 5.7°, dashed line in Fig S9a in the ESI†) locates at about ~650 nm, which corresponds to a red color. This is consistent with the picture in Fig. 3b (letter "N").

The degree of scattering depends not only on the scattering angle but also on the size of the spheres. As shown in Fig. 6b, spheres with an average diameter of 1.65 μm, 1.20 μm and 0.94 μm, obtained with the addition of 40 mM, 120 mM and 140 mM HMTA, scattered *ca.* 650, 500 and 425 nm light and displayed red, blue and purple colors at a low incident angle (letter "N", "M" and "E" in Fig. 5b), respectively. In addition,

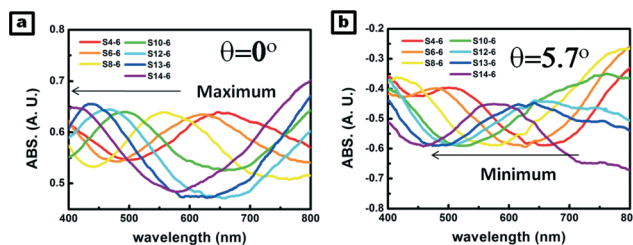Fig. 5 Photographs of transparent plastic slides which were coated with the various-sized spheres by doctor-blade. (a) All the spheres synthesized with different concentrations of HMTA (40–140 mM) have a white color which is similar to general ZnO powders. (b) When a back light is turned on, multicolored words could be observed through the transparent plastic slides by Mie scattering at a scattering angle of θ > 0° (from left to right, red (S4), orange (S6), yellow (S8), green (S10), cyan (S12), blue (S13), and purple (S14), respectively).

Fig. 6 UV-vis absorption spectrum of the various-sized spheres synthesized with different concentrations of HMTA (40–140 mM) at different scattering angles (a) θ = 0° (b) θ = 5.7°.

as the size of spheres decreases, a blue-shift in the local minimum and maximum of the absorption was observed in Fig. 6a and b, respectively. The theoretical Mie scattering spectra of the spheres were calculated by Mie Plot software[20,44] and are presented in Fig. S10 in the ESI.† The simulated curves match the experimental spectra well, although there is a small inconsistency for smaller spheres (S13 and S14) due to a deformed spherical structure with the irregular shell of LBZ.

Mie scattering behavior of the ZnO spheres

As mentioned above, the annealed spheres maintained their spherical structure but exhibited the crystallinity of a wurtzite phase. The reduced volume and the increased refractive index of the spheres had an influence on the Mie scattering properties. As shown in Fig. 7a, the vivid color was still observed when the samples were illuminated under a back light, implying that these ZnO spheres had a Mie scattering property as well. The plastic film coated with S4a, S8a, S12a and S14a displayed orange, blue, purple and violet colors at a low incident angle, respectively. Fig. 7b–e are the absorption spectra of S4a, S8a, S12a and S14a at a scattering angle of $\theta = 0°$, respectively. The ZnO spheres with an average diameter of 1.21 μm (S4a) forward scattered the light with wavelengths of ca. 490 and 775 nm (S4: ~ 500 and 880 nm). A slight blue shift of the local minimum in the absorption spectra of these spheres was found after thermal decomposition. It originated from the shrinking sphere volume (reduced 30% diameter) and the increased refractive index.

Light harvesting is the key factor for new solar energy conversion devices. It has been reported that TiO_2 with a Mie scattering effect has been applied in dye-sensitized solar cells[4] and photoelectrochemical H_2 production[8] to enhance the light utilization efficiency over TiO_2. The lengthened path of the incident light was induced by the scattering effect between uniform TiO_2 spheres with sizes comparable to its wavelength. Therefore, ZnO spheres with characteristics of visible light absorption and scattering are expected to be useful in optical-related applications to increase light harvesting. Moreover, the feature of light selectivity of Mie scattering can also be used in SERS enhancement,[45] and biosensors.[17] Further studies regarding this are in progress.

Conclusions

In summary, we successfully synthesized size-tunable wurtzite ZnO spheres with visible light absorption and scattering properties in a two-step method. Firstly, the nucleation-controlled method with the assistance of a chelating agent was adopted to control the size of amorphous/LBZ spheres by adjusting the HMTA concentration in a reflux reaction. The competition between hydroxyl ions and citrate to the ligand with Zn^{2+} has an influence on the size, uniformity and the crystal phase of the spheres. Secondly, the amorphous/LBZ spheres were further annealed and transformed into wurtzite ZnO spheres with visible absorption. The uniform spheres exhibit Mie scattering behavior in the visible range, and the full absorption spectrum was easily obtained by tuning the size of the spheres. The fascinating optical properties of the ZnO spheres is expected to make them useful for optical-related applications, such as SERS enhancement, dye-sensitized solar cells, and H_2 evolution by increasing light harvesting.

Acknowledgements

Notes and references

1 Z. Dong, X. Lai, J. E. Halpert, N. Yang, L. Yi, J. Zhai, D. Wang, Z. Tang and L. Jiang, *Adv. Mater.*, 2012, **24**, 1046–1049.

2 V. M. Guerin, J. Elias, T. T. Nguyen, L. Philippe and T. Pauporte, *Phys. Chem. Chem. Phys.*, 2012, **14**, 12948–12955.

3 H. Wang, M. Miyauchi, Y. Ishikawa, A. Pyatenko, N. Koshizaki, Y. Li, L. Li, X. Li, Y. Bando and D. Golberg, *J. Am. Chem. Soc.*, 2011, **133**, 19102–19109.

4 I. G. Yu, Y. J. Kim, H. J. Kim, C. Lee and W. I. Lee, *J. Mater. Chem.*, 2011, **21**, 532–538.

5 Q. Zhang, D. Myers, J. Lan, S. A. Jenekhe and G. Cao, *Phys. Chem. Chem. Phys.*, 2012, **14**, 14982–14998.

6 K. Maeda, T. Takata, M. Hara, N. Saito, Y. Inoue, H. Kobayashi and K. Domen, *J. Am. Chem. Soc.*, 2005, **127**, 8286–8287.

7 S. C. Warren and E. Thimsen, *Energy Environ. Sci.*, 2012, **5**, 5133–5146.

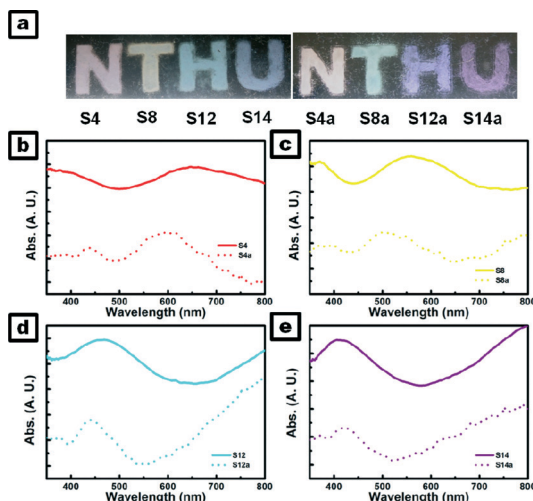

Fig. 7 (a) Photograph of the various-sized spheres before and after annealing. When a back light was turned on, vivid words were still observed through the transparent plastic slides by Mie scattering at a scattering angle of $\theta > 0°$. UV-vis absorption spectrum of the annealed spheres (b) S4a (c) S8a (d) S12a (e) S14a powder coated on transparent plastic slides ($\theta = 0°$).

8 H. Xu, X. Chen, S. Ouyang, T. Kako and J. Ye, *J. Phys. Chem. C*, 2012, **116**, 3833–3839.

9 S. Liu, C. Li, J. Yu and Q. Xiang, *CrystEngComm*, 2011, **13**, 2533–2541.

10 F. Wang, D. Zhao, Z. Xu, Z. Zheng, L. Zhang and D. Shen, *J. Mater. Chem. A*, 2013, **1**, 9132–9137.

11 J. Wang, Z. Wang, B. Huang, Y. Ma, Y. Liu, X. Qin, X. Zhang and Y. Dai, *ACS Appl. Mater. Interfaces*, 2012, **4**, 4024–4030.

12 S. Baruah, S. S. Sinha, B. Ghosh, S. K. Pal, A. K. Raychaudhuri and J. Dutta, *J. Appl. Phys.*, 2009, **105**, 074308.

13 S. Rehman, R. Ullah, A. M. Butt and N. D. Gohar, *J. Hazard. Mater.*, 2009, **170**, 560–569.

14 M. Kong, Y. Li, X. Chen, T. Tian, P. Fang, F. Zheng and X. Zhao, *J. Am. Chem. Soc.*, 2011, **133**, 16414–16417.

15 J. Cao, Y. Zhang, L. Liu and J. Ye, *Chem. Commun.*, 2013, **49**, 3440–3442.

16 Q. Kang, J. Cao, Y. Zhang, L. Liu, H. Xu and J. Ye, *J. Mater. Chem. A*, 2013, **1**, 5766–5774.

17 M.-C. Tsai, T.-L. Tsai, D.-B. Shieh, H.-T. Chiu and C.-Y. Lee, *Anal. Chem.*, 2009, **81**, 7590–7596.

18 G. N. Plass, *Appl. Opt.*, 1964, **3**, 867–872.

19 P. D. García, R. Sapienza, J. Bertolotti, M. D. Martín, Á. Blanco, A. Altube, L. Viña, D. S. Wiersma and C. López, *Phys. Rev. A: At., Mol., Opt. Phys.*, 2008, **78**, 023823.

20 M. C. Tsai, T. L. Tsai, C. T. Lin, R. J. Chung, H. S. Sheu, H. T. Chiu and C. Y. Lee, *J. Phys. Chem. C*, 2008, **112**, 2697–2702.

21 M. Retsch, M. Schmelzeisen, H.-J. r. Butt and E. L. Thomas, *Nano Lett.*, 2011, **11**, 1389–1394.

22 M. Chen, L. Hu, J. Xu, M. Liao, L. Wu and X. Fang, *Small*, 2011, **7**, 2449–2453.

23 M.-C. Wu and C.-S. Lee, *Inorg. Chem.*, 2006, **45**, 9634–9636.

24 L. Zhu, Y. Zheng, T. Hao, X. Shi, Y. Chen and J. Ou-Yang, *Mater. Lett.*, 2009, **63**, 2405–2408.

25 S. Cho, J.-W. Jang, A. Jung, S.-H. Lee, J. Lee, J. S. Lee and K.-H. Lee, *Langmuir*, 2010, **27**, 371–378.

26 P. Gerstel, R. C. Hoffmann, P. Lipowsky, L. P. H. Jeurgens, J. Bill and F. Aldinger, *Chem. Mater.*, 2005, **18**, 179–186.

27 Q. Xie, J. Li, Q. Tian and R. Shi, *J. Mater. Chem.*, 2012, **22**, 13541–13547.

28 N. Tripathy, R. Ahmad, H.-S. Jeong and Y.-B. Hahn, *Inorg. Chem.*, 2011, **51**, 1104–1110.

29 Z. Xia, Y. Wang, Y. Fang, Y. Wan, W. Xia and J. Sha, *J. Phys. Chem. C*, 2011, **115**, 14576–14582.

30 Q. Wu, X. Chen, P. Zhang, Y. Han, X. Chen, Y. Yan and S. Li, *Cryst. Growth Des.*, 2008, **8**, 3010–3018.

31 G. Zhang, X. Shen and Y. Yang, *J. Phys. Chem. C*, 2011, **115**, 7145–7152.

32 I. C. Chang, P.-C. Chen, M.-C. Tsai, T.-T. Chen, M.-H. Yang, H.-T. Chiu and C.-Y. Lee, *CrystEngComm*, 2013, **15**, 2363–2366.

33 M. Ocaña, R. Rodriguez-Clemente and C. J. Serna, *Adv. Mater.*, 1995, **7**, 212–216.

34 H. Morioka, H. Tagaya, M. Karasu, J.-I. Kadokawa and K. Chiba, *Inorg. Chem.*, 1999, **38**, 4211–4216.

35 R. Q. Song, A. W. Xu, B. Deng, Q. Li and G. Y. Chen, *Adv. Funct. Mater.*, 2007, **17**, 296–306.

36 G. G. C. Arizaga, K. G. Satyanarayana and F. Wypych, *Solid State Ionics*, 2007, **178**, 1143–1162.

37 Z. Xia, J. Sha, Y. Fang, Y. Wan, Z. Wang and Y. Wang, *Cryst. Growth Des.*, 2010, **10**, 2759–2765.

38 A. S. Milev, G. S. K. Kannangara and M. A. Wilson, *Langmuir*, 2004, **20**, 1888–1894.

39 T. Zhang, W. Dong, M. Keeter-Brewer, S. Konar, R. N. Njabon and Z. R. Tian, *J. Am. Chem. Soc.*, 2006, **128**, 10960–10968.

40 K. Govender, D. S. Boyle, P. B. Kenway and P. O'Brien, *J. Mater. Chem.*, 2004, **14**, 2575–2591.

41 S. Inoue and S. Fujihara, *Inorg. Chem.*, 2011, **50**, 3605–3612.

42 J. Wang, Z. Wang, B. Huang, Y. Ma, Y. Liu, X. Qin, X. Zhang and Y. Dai, *ACS Appl. Mater. Interfaces*, 2012, **4**, 4024–4030.

43 H. Zeng, G. Duan, Y. Li, S. Yang, X. Xu and W. Cai, *Adv. Funct. Mater.*, 2010, **20**, 561–572.

44 S. M. Scholz, R. Vacassy, J. Dutta, H. Hofmann and M. Akinc, *J. Appl. Phys.*, 1998, **83**, 7860–7866.

45 A. Zenidaka, T. Honda and M. Terakawa, *Appl. Phys. A: Mater. Sci. Process.*, 2011, **105**, 393–398.